Chemical and Process Engineering Research
ISSN 2224-7467 (Paper) ISSN 2225-0913 (Online)
Vol.66, 2024

The Analysis of $Cu_{1-x}Ni_xFe_2O_4$ Nanoferrites' Structural, Morphological, Optical, and Magnetic Characteristics

Nasser K. Hejazy Talaat M. Hammad
Technology & Applied Sciences, Al-Quds Open University, Gaza GFM3+FPW, Gaza Strip, Palestine
Physics Department, Faculty of Science, Al-Azhar University, P.O. Box 1277, Gaza, Palestiene
* E-mail of the corresponding author: naserkhejazy@gmail.com

Abstract
The research centered on utilizing the co-precipitation method to explore the consequences of Ni2+ substitution within Cu1-xNixFe2O4 ($0 \leq x \leq 1$) nanoferrites. This encompassed an examination of their physical and chemical attributes spanning structure, form, optics, and magnetism. Laboratory specimens indicated the exclusive development of spinel crystalline structure through XRD analysis, albeit with minor impurities. Outcomes demonstrated that Ni2+ substitution in Cu1-xNixFe2O4 prompted a reduction in particle dimensions from 20 to 11 nm, while the unchanging lattice measure exhibited a gradual reduction from 8.362 to 8.345 8 Å with amplified Ni2+ ion concentrations. Particle dimensions evaluated by TEM micrographs were akin to those from XRD-tested lab-created samples. Furthermore, FTIR spectra enabled the identification of predominant metal-oxygen bonds within Cu1-xNixFe2O4, unveiling an augmentation in the band gap of nanoferrites from 3.32 to 3.62 eV, attributed to heightened Ni2+ ion content. Conversely, the magnetic attributes of nanoferrites at room temperature were probed using a superconductive quantum interferometer (SQUID) arrangement, exposing an augmentation in copper ferrite's magnetic properties aligned with intensified Ni2+ ion prevalence.
Keywords: Band gap; magnetic properties; nanoferrites; optical properties
DOI: 10.7176/CPER/66-04
Publication date: April 30th 2024

1. Introduction

In recent times, the distinctive electrical and magnetic characteristics of ferrites have sparked widespread research interest [1]. Notably, ferrite nanoparticles exhibit unique magnetism due to their significantly altered surface-to-volume ratio compared to bulk materials. These nanoparticles find utility across a spectrum of applications: gas sensors, electronics, hyperthermia, drug transport, magnetic media, MRI, ferrofluids, lithium-ion batteries, magnetic diagnostics, and beyond [2-6]. Applications like photomagnetic materials, magnetic storage systems, and MRI, particularly in hyperthermia and drug delivery, often involve spinels like MFe2O4 (where M(II) = Fe(II), Mn(II), Co(II), Ni(II)) [7-10].Scientists analyze the size and distribution of metal ions at tetrahedral and octahedral sites in the spinel structure and the chemical classification of the divalent metal to determine the composition of ferrites [11, 12]. The formula MFe2O4 characterizes spinel ferrites, where M is a divalent metal and Fe is in the +3 oxidation state [13-16]. Two spinel ferrite structures exist: normal and inverse [17, 18]. Normal spinel features M2+ ions in tetrahedral sites and Fe3+ ions in octahedral sites [19, 20].

The inverse spinel arrangement represents a departure from the conventional spinel structure. In the inverse variant, all M2+ ions, in combination with half of the Fe3+ ions, find their place within the occupied octahedral sites. In contrast, the remaining Fe3+ ions occupy the already taken up tetrahedral sites. This structural disparity gives rise to distinctive physical characteristics.

Notably, the physical properties of ferrites undergo a marked transformation through the strategic substitution of diverse magnetic ions at sites denoted as A and B. This substitution process is underpinned by the intricate ability to effectively manage the distribution of metal ions, allocating them across the available sites within the structure. This intricate interplay among ion substitution, distribution, and structure manifests in significant and discernible variations across the spectrum of physical attributes exhibited by ferrites.

Nickel copper ferrite, a representative of ferrite family, exhibits a foundational spinel structure that lays the groundwork for other ferrite variations [21]. The spatial arrangement of ions within the tetrahedral and octahedral lattice sites, coupled with magnetic interactions, decisively governs the structural and magnetic attributes of spinel ferrites [22]. This is illustrated by the compositional formula (Fe3+)(Ni2+Fe3+)O4 (B), wherein half of the iron atoms occupy tetrahedral sites (A), while an equal proportion of magnetic atoms populate octahedral sites (B). The tetrahedral locale (A) exclusively hosts Fe3+ ions, whereas the octahedral site (B) accommodates both Fe3+ and Ni2+ ions. Consequently, an arrangement of antiparallel spins ensues between Fe3+ and Ni2+ at the tetrahedral site, culminating in a state of ferrimagnetism at the level of octahedral occupancy.

The preparation method distinctly influences the physical attributes of spinel ferrites. Hence, the selection of a suitable synthesis approach is pivotal in ensuring the production of high-quality ferrite nanoparticles [24]. A plethora of techniques, such as chemical co-precipitation, sol-gel, ball milling, citrate precursor,

mechanochemical, glycine nitrate, adjusted oxidation, hydrothermal, and solid-state methods, have been documented in literature for fabricating nickel copper mixed ferrite nanoparticles [25-28].

Among the various synthesis techniques mentioned, co-precipitation stands out as the optimal choice for generating nickel-copper mixed ferrite nanoparticles. This method involves employing a precipitating agent to simultaneously precipitate multiple metal salts within a solution, subsequently followed by heat treatment to disintegrate the formed precipitate [29]. Co-precipitation brings forth several advantages in comparison to alternative methods, including superior dispersion of metal ions within the resulting ferrites, cost-effectiveness, and enhanced control over stoichiometry [30, 31].

Numerous investigations have highlighted the correlation between nickel-copper ferrite substitution and heightened magnetization levels, with increased nickel content being linked to this phenomenon. To illustrate, Saleem et al. conducted a study involving Cu1-xNixFe2O4 nanoparticles, observing a rise in saturation magnetization upon Ni addition, concurrently verifying the formation of a unified cubic structure. In a separate study, Doha et al. employed the co-precipitation ultrasonic irradiation technique to craft Cu1-xNixFe2O4 nanopowders, featuring grain diameters spanning 20 to 30 nm, and attaining a peak magnetization saturation of 73.5 emu/g at x=0.5. Additionally, Azadmanjiri et al. synthesized Cu1-xNixFe2O4 nanoferrites through the sol-gel auto-combustion method.

Furthermore, substituting nickel with copper led to a decline in saturation magnetization (Ms) alongside an elevation in the magnetic anisotropy constant (K). The magnetic traits of CuxNi1-xFe2O4 are profoundly influenced by the synthesis approach and variables like temperature and pH. Vargas-García et al.'s study [38] showcased how the sol-gel method's magnetic properties for CuxNi1-xFe2O4 nanoparticles were subject to the pH of the reaction mixture, with higher pH levels correlating to elevated Ms values. In sum, by manipulating synthesis methods, parameters, and adjusting copper and nickel levels, the electromagnetic characteristics of CuxNi1-xFe2O4 can be fine-tuned.

It seems that more research is needed to explore the magnetic and optical properties of $Cu_{1-x}Ni_xFe_2O_4$ nanoferrites. Although some studies have investigated the impact of nickel content on the magnetic properties of the compound, the relationship between the composition and optical properties of $Cu_{1-x}Ni_xFe_2O_4$ remains largely unexplored. Future research in this area may help to identify potential applications of $Cu_{1-x}Ni_xFe_2O_4$ nanoferrites in fields such as magnetic data storage, electromagnetic wave absorption, and optoelectronics.

The research study utilized the precipitation method to create nanoparticles of $Cu_{1-x}Ni_xFe_2O_4$ with varying amounts of nickel substitution (x= 0.2, 0.4, 0.6, 0.8, and 1.0). The aim was to investigate the effect of nickel substitution on the structural, magnetic, and optical properties of the nanoparticles

2. Materials and methods

Using the precipitation technique, copper ferrite nanoparticles doped with nickel were synthesized [38]. For nanoparticle creation, specific concentrations of nickel sulfate (NiSO4.6H2O), copper sulfate pentahydrate (CuSO4.5H2O), and ferrous ammonium sulfate (NH4)2Fe(SO4)2.6H2O were dissolved in deionized water. After intense stirring for 60 minutes, oxalic acid (20 mmol) was gradually added and stirred for another hour. The ensuing (Cu, Ni, Fe) oxalate precipitate underwent multiple water rinses and was dried at 100°C for 24 hours. Subsequently, the dried substance was annealed at 500°C in a muffle furnace for three hours, culminating in the formation of Cu1-xNixFe2O4 nanoparticles.

2.1 Characterization

The XRD powder analysis of the sample's crystal structure was conducted using CuK wavelength (=1.5) radiation on the XDS 2000 X-ray diffractometer from Scintac Inc., USA, at ambient temperature. For chemical analysis, Fourier-transform infrared spectroscopy (Frontier Perkin Elmer) was employed to discern the chemical bonds within the sample. Optical absorption traits and band gap energy were ascertained via UV-Vis absorption spectroscopy (Hewlett Packard 8453), while luminescence was assessed using fluorescence spectrophotometry (Perkin-Elmer LS 50B). Nanoparticle morphology was examined using the Tecnai F300 transmission electron microscope (TEM). Moreover, magnetism investigations of the produced nanoferrites utilized the Quantum Design MPMS XL-7 magnetometer in RSO mode, encompassing field-dependent magnetization tests under fields up to 40 KOe.

3. Results

3.1. Structural analysis

The X-ray diffraction patterns of the $Cu_{1-x}Ni_xFe_2O_4$ samples are shown in Figure 1. The peaks observed in the XRD spectra correspond to the (220), (311), (400), (422), (511), and (440) planes at 2θ angles of 29.8, 35.46, 43.74, 53.86, 56.78, and 62.32 degrees, respectively.

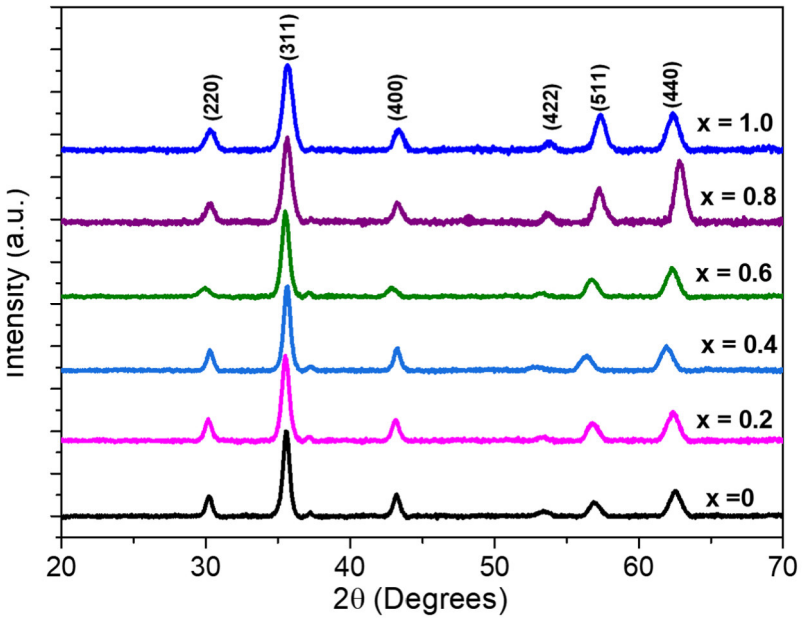

Figure 1: XRD analysis of $Cu_{1-x}Ni_xFe_2O_4$ nanoferrites.

The XRD patterns in Fig. 1 indicate that all samples of $Cu_{1-x}Ni_xFe_2O_4$ have a cubic spinel lattice structure with no impurity phases (such as Fe_2O_3, NiO, CuO, etc.). As the concentration of Ni ions increases, the intensity of the peaks decreases, particularly for the (311) reflection. The sharp and narrow peaks suggest that the precipitation technique used in this study produces highly pure nanoferrites [39-41]. The width of the diffraction peaks increases with an increase in Ni^{2+} ion concentration. The lattice constant can be calculated using the following equation.

$$\frac{1}{d^2} = \frac{h^2+k^2+l^2}{a^2}$$

In the context of this discussion, (hkl) represents Miller indices, 'd' symbolizes interplanar spacing, and 'a' denotes the lattice constant. Tabulated in Table 1 are results from XRD spectral analysis, revealing the lattice constant and crystallite size. With an increase in Ni concentration, the lattice constant exhibited a decrease from 8.362 to 8.345. The application of the Debye-Scherrer formula yielded an average crystallite size ranging between 20 and 11 nm. Table 1 underscores the simultaneous reduction in particle size and lattice constant with rising Ni concentration. The determination of crystallite size utilized the (311) peak.

Composition	Lattice Constant (A)	Particle size (nm)
0.0	8.362	20
0.2	8.359	18.4
0.4	8.357	16.7
0.6	3.352	14.5
0.8	8.349	13.2
1.0	8.342	11

Table 1 Lattice constant and particle size of $Cu_{1-x}Ni_xFe_2O_4$

Illustrated in Fig. 2 is a correlation between mean crystallite size and lattice parameter concerning nickel content. With a rise in Ni2+ ion concentration, the lattice parameter declines, accompanied by a reduction in mean crystallite size. This relationship adheres to Vegard's law, stipulating a linear link between solid solution unit cell characteristics and composition. The data in Fig. 2 proposes Ni2+ ion substitution for Cu2+ ions within the copper ferrite structure, contributing to diminished lattice parameter and crystallite size.

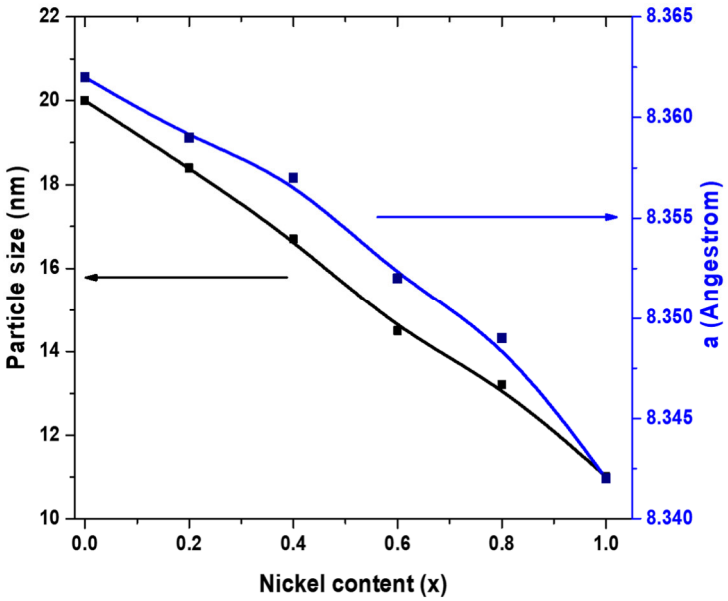

Figure 2: Variation of average particle size and Lattice parameter as a function of Ni content.

The augmented Ni ion concentration in copper nanoferrites corresponds to reduced average crystallite size. This outcome is ascribed to the smaller ionic radius of Ni2+ ions (0.69) compared to Cu2+ ions (0.73), thereby inducing a decreased lattice parameter. This observation aligns with prior predictions.

3.2. FT-IR analysis

The ideal spinel configuration comprises two distinct sub-lattices: tetrahedral sites (A) and octahedral sites (B). Varying combinations of metal cation charges are allocated across these sub-lattices. This distribution of metal ions within A and B sites holds pivotal significance in establishing the magnetic attributes of spinel ferrite. The magnetic traits of Cu1-xNixFe2O4 nanofibers undergo alteration due to the exchange of Ni2+ ions for Cu2+ ions at the B sites. By analyzing FT-IR spectra connected to ion vibrations within the crystal lattice, the placements of Ni2+, Cu2+, and Fe3+ ions within the spinel framework can be deduced. Fig. 3 illustrates the Cu1-xNixFe2O4 FTIR spectra spanning 400 to 3000 cm-1 (x=0.0, 0.2, 0.6, and 1.0).

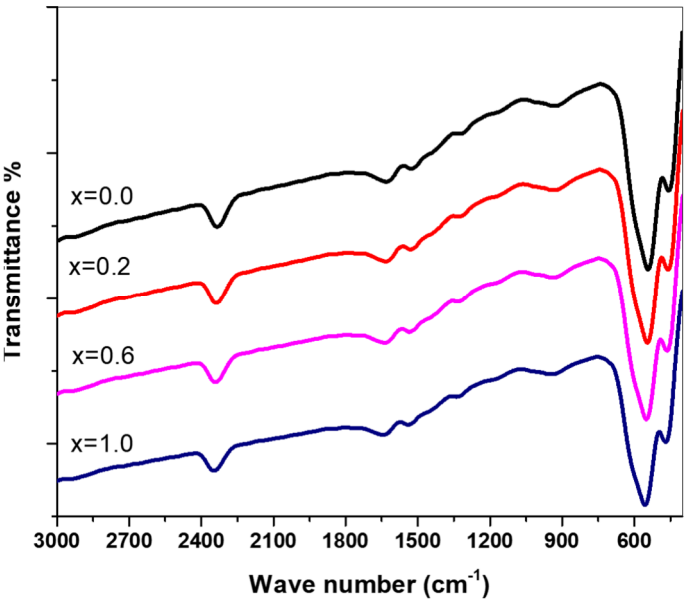

Figure 3: FT-IR spectra of $Cu_{1-x}Ni_xFe_2O_4$ (a) x = 0.0, (b) x = 0.2, (c) x=0.6 and (d) x=1.0

To gain further insights into sample structure and bonding, the infrared transmittance spectra of the synthesized samples were scrutinized. Mixed ferrites exhibit extensive metal-oxygen bands originating from both tetrahedral (A-site) and octahedral (B-site) locations. The v1 band, linked predominantly to intrinsic stretching vibrations of metal and oxygen atoms at the tetrahedral site, commonly manifests within 542 to 555 cm-1 (Mtetra-O). Conversely, the lowest band 2 typically corresponds to stretching vibrations of the metal at the

octahedral site, falling between 454 and 470 cm-1 (Mocta-O) [45]. Our FTIR spectra align with earlier investigations [23,50]. Fe3+-O2 bond length disparities at A and B sites may stem from differing ν1 and ν2 band positions. Notably, Fe-O distance proves shorter at A sites (1.89) than at B sites (2.03) [24,46]. Substituting Cu2+ ions with Ni2+ ions might prompt certain Fe3+ ions to shift from A to B sites due to charge imbalance, thereby amplifying the Fe3+-O2 stretching vibration.

3.3 Transmission electron microscopy (TEM) studies

The morphology and histograms of the $Cu_{1-x}Ni_xFe_2O_4$ system (x= 0.2, 0.4, 0.6, 0.8, and 1.0) are shown in Figures 4 and 5.

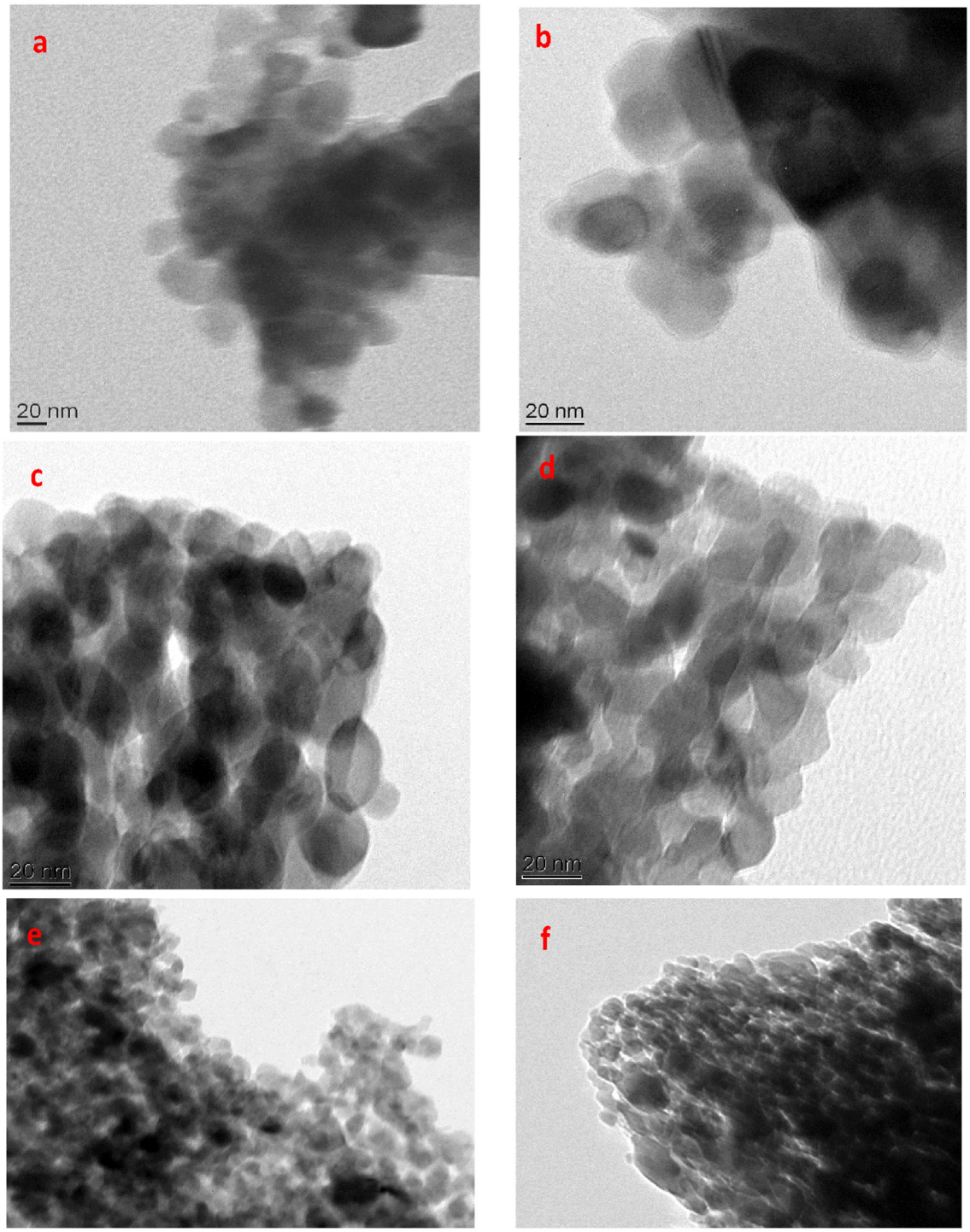

Figure 4. TEM micrographs of $Cu_{1-x}Ni_xFe_2O_4$ (a) x= 0.0, (b) x= 0.2, (c) x= 0.6 and (d) x= 0.8 and (e) x= 1.0.

F

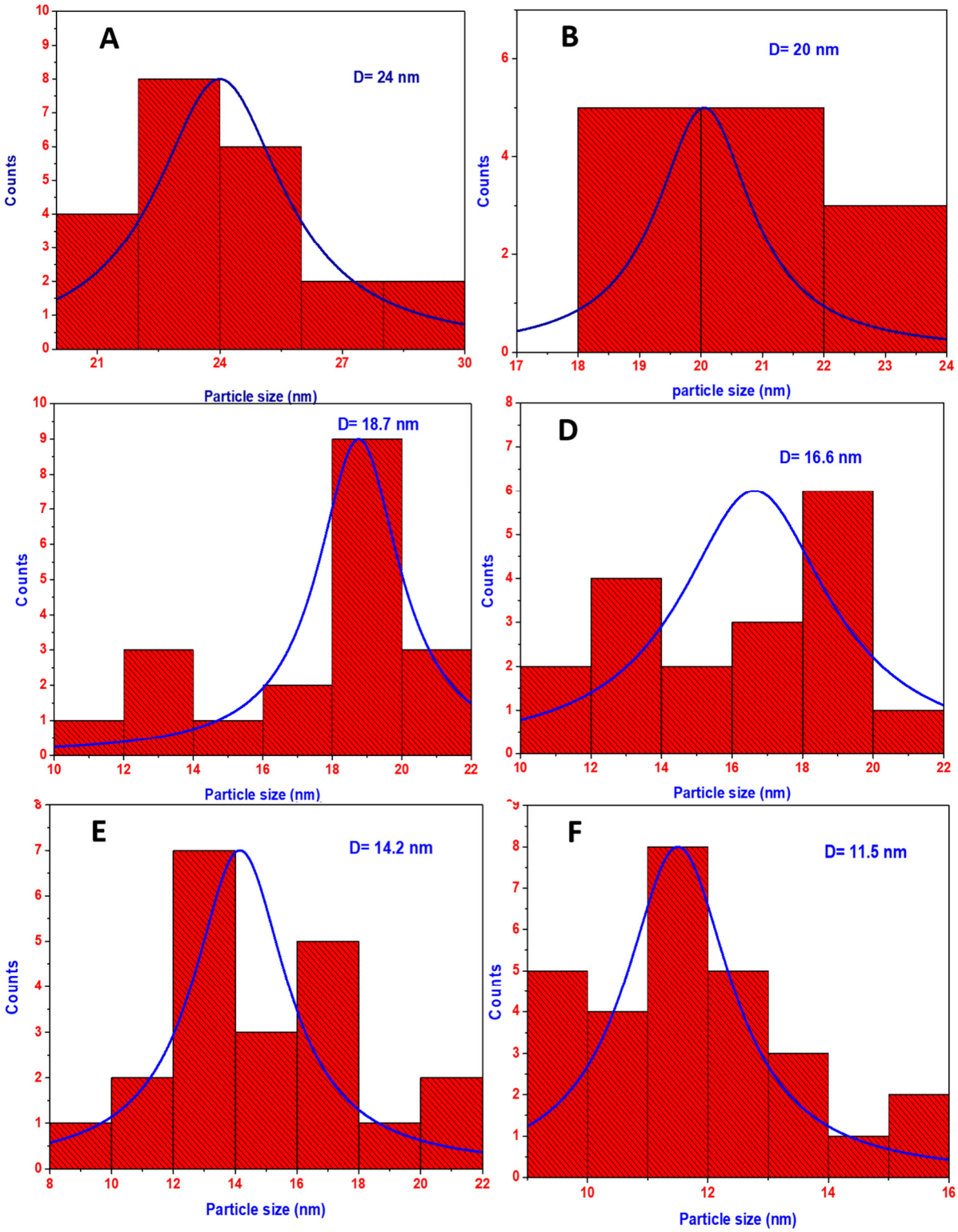

Figure 5: Histograms of $Cu_{1-x}Ni_xFe_2O_4$ (a) x= 0.0, (b) x= 0.2, (c) x= 0.6 and (d) x= 0.8 and (e) x= 1.0.

TEM images of each Cu-Ni sample showcased spherical particles, as illustrated in Fig. 4(a-f). CuFe2O4 nanoparticle purity was confirmed in Fig. 5A, while Fig. 4(b-f) exhibited uniform and clustered Cu-Ni nanoferrires. Particle clustering emerged due to magnetic particle interactions [47]. Fig. 5 (a-f) displayed histograms for Ni-doped CuFe2O4 samples, unveiling average particle sizes spanning 24 to 11.5 nm. Fig. 5 outcomes indicated a size decrease in Cu1-xNixFe2O4 nanoparticles as nickel concentration rose, harmonizing with crystallite sizes deduced from XRD data.

3.4 Energy dispersive X-ray spectroscopy (EDX) analysis

Fig. 6 displays results from EDX analysis, examining nanoparticles with varying nickel concentrations (x= 0.2, 0.4, 0.6, 0.8, and 1.0) to ascertain chemical composition. Pure CuFe2O4 EDX spectra (Fig. 6a) depict peaks corresponding to Fe, Cu, and O elements. Ni-doped CuFe2O4 sample EDX spectra (Fig. 6(b-e)) feature peaks linked to Fe, Cu, Ni, and O elements. EDX data aligns with XRD outcomes, affirming successful mixed ferrite formation under experimental conditions. These findings imply the coexistence of CuFe2O4 and Ni-doped CuFe2O4 impurities.

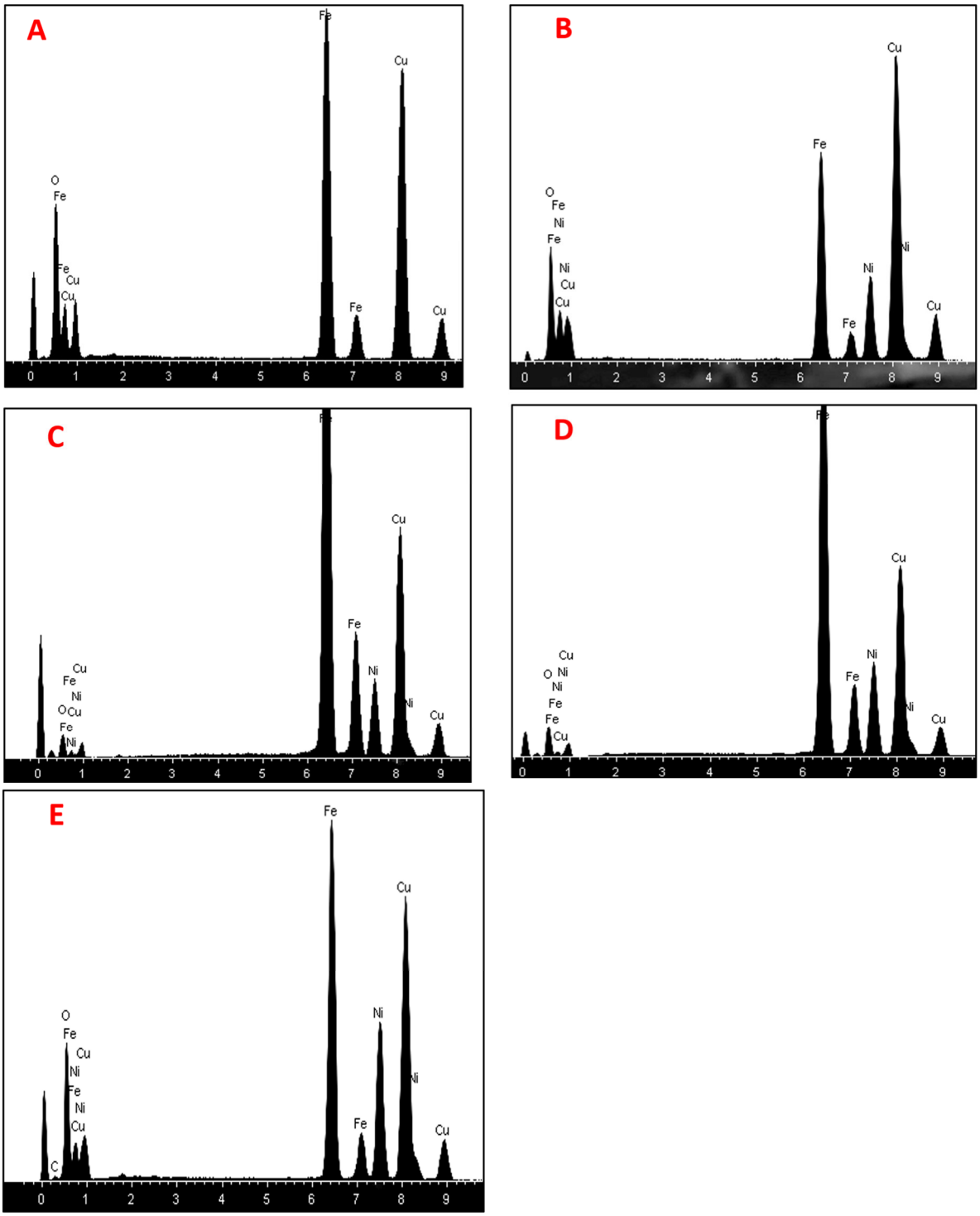

Figure 6: EDX spectrum of $Cu_{1-x}Ni_xFe_2O_4$ (a) x = 0.0, (b) x = 0.2, (c) x = 0.4, (d) x= 0.6 and (e) x = 0.8.

3.5 UV-Vis absorption studies

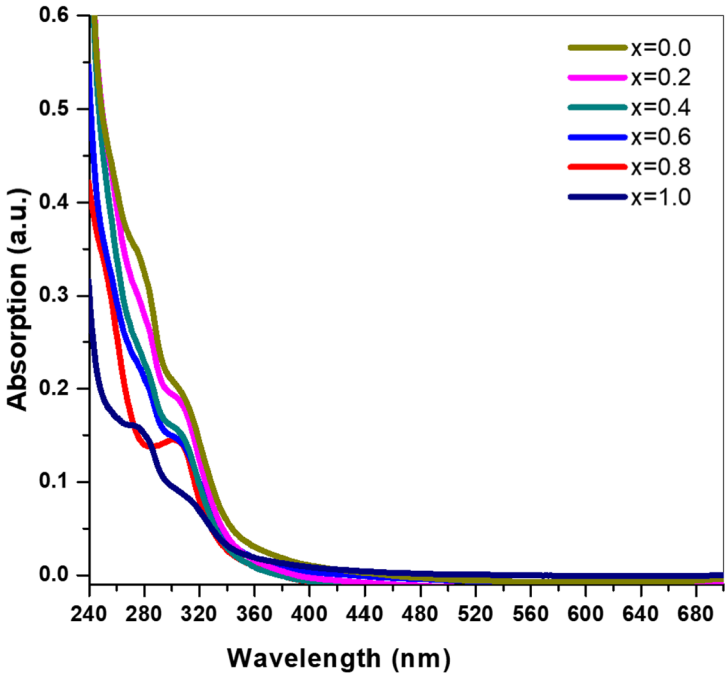

Figure 7: UV-vis. spectra of $Cu_{1-x}Ni_xFe_2O_4$ (x= 0.0, 0.2, 0.4, 0.6, 0.8 and 1) system.

The figure 7 shows the UV-Vis optical spectra of $Cu_{1-x}Ni_xFe_2O_4$ nanoferrites, which were measured in the range of 240 nm to 700 nm.

Fundamental absorption pertains to optical absorption, occurring when material electrons shift from the valence to the conduction band upon photon absorption meeting or exceeding the material's band gap energy. This process generates electron-hole pairs, influencing material's electrical and optical characteristics. In Cu1-xNixFe2O4 ferrite nanoparticles, Ni substitution for Cu elevates band gap energy, evident in UV-Vis spectra's absorption band shift to shorter wavelengths. Tauc's relation, linking material's absorption coefficient and band gap energy, facilitates calculation of band gap energy for the prepared samples. For prepared samples, the linear extrapolation of Tauc's relation [48] produced the optical band gap energy (Eg) as follows: (2)

$$(\alpha h\nu) = \sqrt{A(h\nu - E_g)} \qquad (2)$$

Figure 8 displays a graph depicting (αhν)2 plotted against energy (hν), facilitating the determination of the direct electronic transition energy gap (Eg) in Cu1-xNixFe2O4 nanoferrites. The optical band gap energy (Eg) was derived by extrapolating the linear segment of the curve to (αhν)2 = 0, utilizing the Tauc plot methodology [48]. The gradient of this linear segment was computed through the Tauc plot approach. Computed values of the optical band gap energy (Eg) for Cu1-xNixFe2O4 nanoparticles, featuring distinct Ni concentrations, are detailed in Table 1. The data showcased in the table indicates an elevation in optical band gap energy with growing Ni concentration in the samples, a trend that harmonizes with UV-Vis spectroscopy findings. The Cu1-xNixFe2O4 nanoparticles' optical band gap energy is notably responsive to varying Ni ion concentrations. The augmented band gap energy signifies that replacing Cu2+ ions with Ni2+ ions curtails available valence band electrons, hence boosting the band gap energy. This phenomenon stems from dissimilarities in the 3d orbital energies of Cu2+ and Ni2+ ions, prompting adjustments in the material's electronic configuration and impacting the band gap energy.

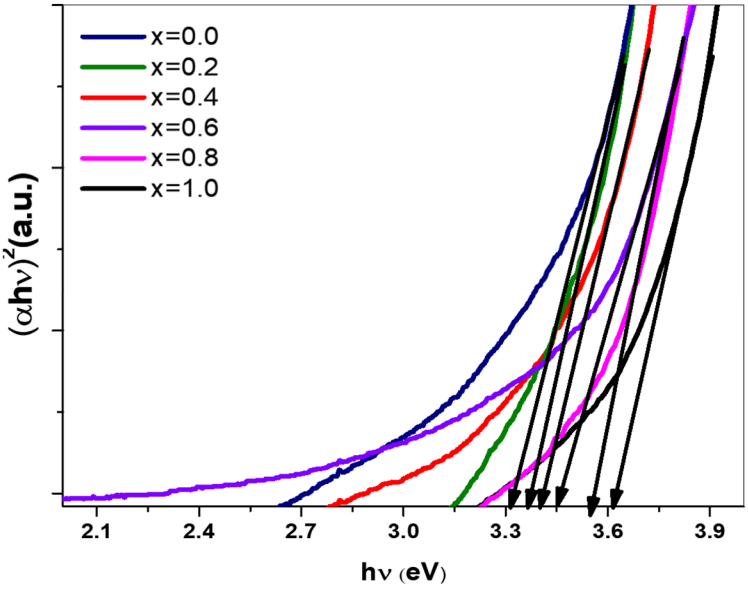

Figure 8: Energy gap spectra of $Cu_{1-x}Ni_xFe_2O_4$ nanoferrite.

The band gap energy within the Cu1-xNixFe2O4 system spanned from 3.32 to 3.62 eV, where copper ferrite exhibited 3.32 eV and nickel ferrite showcased 3.62 eV. This outcome adhered to Bras' effective mass model, revealing an inverse correlation between measured band gap and particle size. The introduction of more Ni2+ content triggered heightened band gap energy, a trend documented by other scholars. The surge in optical band gap owes itself to diverse factors like impurities, carrier densities, crystallite thickness, and lattice strain, all potentiated by the infusion of Ni2+ ions into CuFe2O4 ferrites. These fluctuations in band gap originate from intricate sp-d interactions among CuFe2O4 and band electrons, alongside localized d electrons of divalent nickel ions.

3.6 Magnetic Measurements

For substituting Cu2+ ions within the spinel structure, Ni2+ was deliberately selected due to its affinity for the octahedral B site, driven by its inherent magnetism. Prior investigations into nickel-copper ferrites underscored that while Cu2+ ions occupy both A and B sites, Ni2+ ions are exclusively confined to the octahedral region. The configuration of cations within the tetrahedral and octahedral sites, alongside their magnetic interactions, exerts a significant influence on the structural and magnetic attributes of spinel ferrites. In the present study, magnetic hysteresis loops of Cu1-xNixFe2O4 (x=0.0, 0.2, 0.4, 0.6, 0.8, and 1.0) were measured at room temperature using SQUID, revealing, as illustrated in Fig. 9, that the nanoferrites showcase characteristics of soft magnetism.

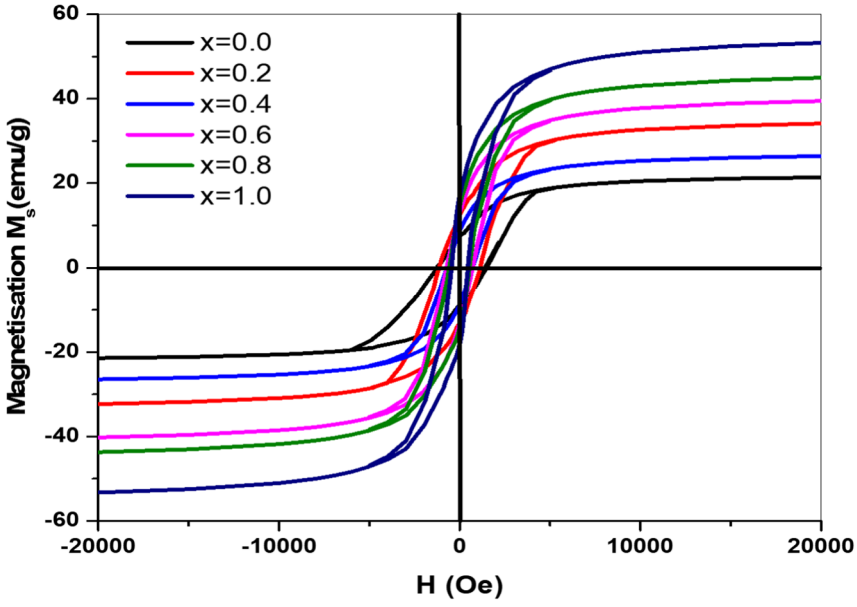

Figure 9: Magnetic hysteresis loops of $Cu_{1-x}Ni_xFe_2O_4$ (x = 0.0, 0.2, 0.4, 0.6 and 0.8) system.

Table 2 lists the different parameters, including saturation magnetization (Ms), remanent (Mr), coercivity (Hc), (Mr / Ms), and magnetic moment (B).

Table 2 The values of magnetic parameters, Ms, Mr, Hc, Mr/Ms and ηB of $Cu_{1-x}Ni_xFe_2O_4$ nanoparticles at x= 0, 0.2, 0.6, 0.8, and 1.0

X	Saturation magnetization M_s (emu/g)	Remanent magnetization M_r (emu/g)	Coercivity H_c (Oe)	M_r/M_s	Magnetic moment ηB (μ_B)
0	20.35	7.26	1330	0.36	0.872
0.2	26.6	8.8	1136	0.48	1.14
0.4	34.8	12.5	730	0.45	1.5
0.6	40.2	13.3	700	0.25	1.72
0.8	45.7	14.8	576	0.18	1.96
1.0	54.3	17.05	456	0.024	2.11

According to the ferrite cation distribution, an increase in Ni^{2+} concentration causes Ms to increase and Hc to decrease (see Fig. 10).

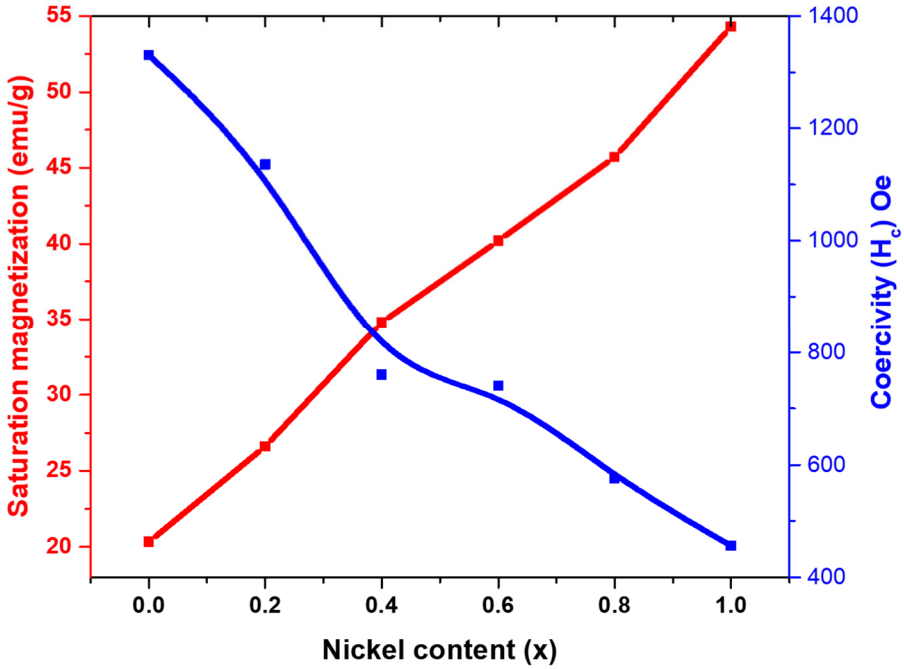

Figure 10: Saturation magnetization Ms and coercivity H_c versus copper content x in $Cu_{1-x}Ni_xFe_2O_4$.

Observations have highlighted a noticeable augmentation in both saturation magnetization (Ms) and remanent magnetization (Mr) with escalating nickel substitution. The shift from x=0 to x=1.0 triggers an upsurge in saturation magnetization, soaring from 20.35 to 54.3 emug-1, a trend evident in both Table 2 and Figure 10. This elevation in saturation magnetization is attributed to the heightened magnetic moment (2.3 B) of Ni2+ ions in contrast to the 1 B magnetic moment of Cu2+ ions [61]. Intrinsically linked to Ni2+ ion doping, the magnetic moment of the samples experienced an overall increase, harmonizing with the sequential rise in magnetic moment within the B-sub lattice due to incremental nickel doping. The escalation in Ms due to Ni2+ content rise can be elucidated by the potential substitution of Ni2+ for Cu2+ at tetrahedral sites. Patterns in Ms variation can be justified through Neel's model, determining magnetization (B) as M(B) = MB - MA, where MA and MB represent net magnetic moments at A (tetrahedral) and B (octahedral) sites, respectively.

The introduction of Ni2+ ions at the A-site prompts the migration of Fe3+ ions from A to B sites, augmenting Fe3+ concentration at B-sites and, consequently, B-site magnetic moment. This elevates the number of spins at the B site, culminating in heightened net magnetization. Nonetheless, an escalation in Ni2+ level also corresponds to an amplified super-exchange interaction between A and B sites. The increase in saturation

magnetization might arise from the intensified exchange interaction between A and B sites. Therefore, the increase in saturation magnetization and magnetic moment is consistent with the predicted increase in $Cu_{1-x}Ni_xFe_2O_4$ nanoferrites [33]. The following relationship is computed [65] and shown in Table 2 to calculate the magnetic moment (B) in Bohr.

$$\eta_B = \frac{M \times M_S}{5585} \quad (4)$$

Where "Ms" stands for saturation magnetization and "M" stands for molecular weight. Strong super-exchange interactions between the various sites increased the values. In our example, was seen to rise along with the saturation magnetization when Ni^2 content increased (see Fig. 11). Additionally, the ratio of Mr to Ms (Mr/Ms) declined as Ni content inclined. For ferrites $Cu_{1-x}Ni_xFe_2O_4$ with Mr/Ms values ranging from 0.36 to 0.024, see Table 2.

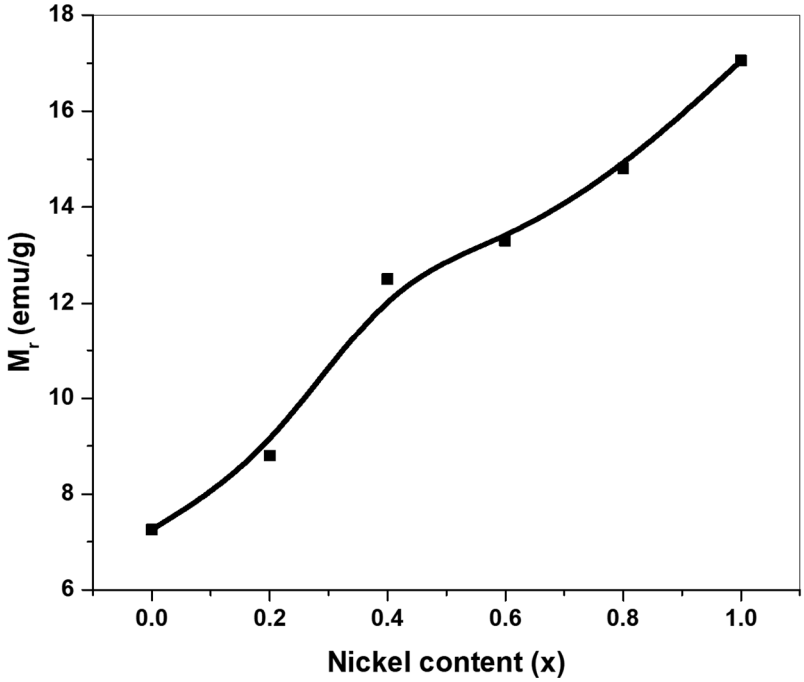

Figure 11: M_r versus copper content x in $Cu_{1-x}Ni_xFe_2O_4$

The recorded values fall short of the anticipated unity (1.0) standard for single-domain ferromagnetic samples. The variation in particle sizes within the material could have triggered inter-grain interactions, explaining the deviation from the expected value (1) [66–68].

4. Conclusion

Cu1-xNixFe2O4 nanoferrites were synthesized through co-precipitation to investigate the impact of nickel substitution on copper ferrites' physical characteristics. The optical, electrical properties, and grain size were notably affected by diverse Ni-doped copper ferrite compositions. XRD and FTIR analyses confirmed a singular-phase cubic spinel structure, revealing reduced lattice constant with elevated Ni concentration due to its smaller radius, accompanied by particle size variations. A reduction in the nanoparticle sizes was detected from 20 to 11 nm as the nickel concentration increased. With the addition of more nickel ions, the band gap energy of nanoferrites rises from 3.32 to 3.62 eV. Furthermore, when nickel ions replace copper ions, saturation magnetization, and remanent magnetization steadily increased. Future applications are suggested based on the results of the synthesized nanoferrites modifications and their physical properties.

5. References

1. Gaba, S. et al. (2018). Influence of La3+ ion doping on physical properties of magnesium nanoferrite for microwave absorption application. *J. Magn. Magn. Mater.* 460, 69-77
2. Kefeni, K. K., Msagati, T. A. M., & Mamba B. B. (2017). Ferrite nanoparticles: synthesis, characterization and applications in electronic device. *Mater. Sci. Engg.* B 215, 37-55
3. Hammad, Talaat M. et al. (2016) Influence of pluronic P123 in modifying the morphological and optical properties of PbS nanocomposite `` *J Mater Sci: Mater Electron*. 27, 4186–4193
4. Sundararajan, M et al. (2017). Photocatalytic degradation of rhodamine B under visible light using nanostructured zinc doped cobalt ferrite: Kinetics and mechanism. *Ceram. Int.* 43, 540-548

5. Akhtar, M. N., et al. (2017). Structural, spectral, dielectric and magnetic properties of nanosized ferrite for microwave absorption and high frequency applications. *Ceram. Int*. 43, 4357- 4365
6. Pour, S. A., et al. (2017). Carboxymethyl cellulose (CMC) loaded Co-Cu doped manganese ferrite nanorods as a new dual modal simultaneous contrast agent for magnetic resonance imaging and nanocarrier for drug delivery system. *J. Magn. Magn. Mater.* 438, 85-94
7. Mohapatra, J., et al. (2013). Surface controlled synthesis of MFe2O4 (M= Mn, Fe, Co, Ni and Zn) nanoparticles and their magnetic characteristics. *Cryst. Eng. Comm,* 15, 524-532
8. Patade, S.R., et al. (2020). Preparation and Characterizations of Magnetic Nanofluid of Zinc Ferrite for Hyperthermia Application. *Nanomaterials and Energy* 9, 1-7
9. Hammad, T. M. et al. (2015). 'Optical properties of Cu2+ and Fe2+ doped ZnS semiconductor nanoparticles synthesized by co-precipitation method'' *J Mater Sci: Mater Electron* 26, 5495- 5501.
10. Hammad, T. M. et al. "comprehensive study of the impact of Mg2+ doping on optical, structural, and magnetic properties of copper nanoferrites," *Journal of Superconductivity and Novel Magnetism.* https://doi.org/10.1007/s10948-020-05559-2
11. Hammad, T. M. et al. (2021). "Investigation of structural, optical, and magnetic properties of Co2+ ions substituted CuFe2O4 spinel ferrite nanoparticles prepared via precipitation approach," *Journal of the Australian Ceramic Society*, 57, 543-553.
12. Bharati, V., et al. (2020). Influence of trivalent Al–Cr co-substitution on the structural, morphological and Mössbauer properties of nickel ferrite nanoparticles. *Journal of Alloys and Compounds,* 821, 153501
13. Manikandan, A., Judith Vijaya, J. & Kennedy, L. John. (2013). *Phys*. E, 49, 117–123
14. Maruthamani, S. et al. (2017). *J. Colloid Interface Sci.,* 498, 449-459
15. Asiri, S. et al. (2018). Ceram. Int., 44, 5751–5759
16. Mathubala, G. (2016). et al. *Nanosci. Nanotechnol. Lett.,* 8, 375–381
17. Bayoumi, W. (2012). *J. Mater. Sci.,* 2007, 42, 8254–8261. 18 N. M. Deraz and A. Alari, J. Anal. Appl. Pyrolysis 94, 41–47
18. Silambarasu, A., Manikandan, A. & Balakrishman, K. (2017). *J. Supercond. Novel Magn.,* 30, 2631–2640
19. Ravichandran, A. T. et al. (2018). *Ceram. Int.,* 44, 13247–13252
20. Rajmohan, S. et al. (2016). *Nanosci. Nanotechnol. Lett.,* 8, 393–398
21. Bragg, W.H. (1915). *Philos. Mag.* 30, 305
22. Shirsath, S.E., Toksha, B.G. & Jadhav, K. M. (2009). *Mater. Chem. Phys.* 117, 163
23. Al-Ghamdi, A. A., et al. (2017). "Evolution of the structure, magnetic and optical properties of Ni1-xCuxFe2O4 spinel ferrites prepared by soft mechanochemical method." *J. Alloys Compd.* 712, 82-89
24. Skandan. G., et al.(1994). "Ultrafine-Grained Dense Monoclinic and Tetragonal Zirconia." *J. Am. Ceram. Soc.* 77, 1706
25. Boobalan. T., et al. (2017). "Preparation and characterization of polyol assisted ultrafine Cu-Ni-Mg-Ca mixed ferrite via co-precipitation method." J. *Magn. Magn. Mater.* 428, 382-389
26. Babu, K. R., Rao, K. R. & Babu, B. R., (2017). Cu2+ - modified physical properties of cobalt-nickel ferrite. *J. Magn. Magn. Mater.* 434, 118-125
27. Das, P. S. & Singh, G. P. (2016). Structural, magnetic and dielectric study of Cu substituted NiZn ferrite nanorod. *J. Magn. Magn. Mater.* 401, 918-924
28. Gholizadeh, A. & Jafari, E. (2017). Effect of sintering atmosphere and temperature on structural and magnetic properties of Ni-Cu-Zn ferrite nano-particles: Magnetic enhancement by a reducing atmosphere. *J. Magn. Magn. Mater.* 422, 328-336
29. Bammannavar, B. K., Naik, L. R. & Pujar, R. B. (2008). *Prog. Electromagnet. Res. Lett.,* 4, 121–129
30 Mohseni,. H., et al. (2012). Magnetic and structural studies of the Mn-doped Mg–Zn ferrite nanoparticles synthesized by the glycine nitrate process, *J. Magn. Mater. Mater.* 324, 3741-3747
31. Lontio, R. et al. (2015). *J. Solid State Chem.,* 230, 381–389
32. Thanh, Nguyen Kim, et al. (2016). Cation distribution in CuFe2O4 nanoparticles: Effects of Ni doping on magnetic properties, *JOURNAL OF APPLIED PHYSICS*, 120, 142115
33. Saleem, Adil, et al. (2020). *Mater. Res. Express,* 7, 016117
34. Doha, S.G., et al. (2004). *J. Magn. Magn. Mater.* 272–276, 2238
35. Azadmanjiri, J. et al. (2007). *Mater. Lett.* 61, 84
36. Roumaih, Kh. (2008). *J. Alloys Compd.* 465, 291
37. Msomi, J. & Moyo, T. (2009). *J. Magn. Magn. Mater.* 321, 1246
38. Hammad, T. M., et al. (2018). *Journal of Alloys and Compounds,* 741, 123-130
39. Tehrani, F.S. et al. (2012). *J. Supercond. Novel Magn*. 25, 2443–2455
40. Luadthong, C. et al. (2013). *Mater. Chem. Phys*. 143, 203–208
41. Masti, S.A., Sharma, A.K. & Vasambekar, P.N. (2013). *Adv. Appl. Sci. Res.* 4, 163–166
42 Pankhurst,. Q. A. et al. (2003). *J. Phys.D: Appl. Phys.* 36, R167

43. Jiang, J. Z. et al. (1999). *Nanostructured Materials,* 12, 737
44. Thanh, Nguyen Kim et al. (2016). *JOURNAL OF APPLIED PHYSICS,* 120, 142115
45. Naidu, V. (2011). Study of Electrical & Magnetic properties in Nanosized Ce-Gd Doped Magnesium Ferrite. *Int. J. Computer Appl.* 27, 0975
46. Mazen, S.A. et al. (1992). *Phys. Status Solidi* (a) 134, 26
47. Rahman, S. et al. (2013). Structural and magnetic properties of ZnMg-ferrite nanoparticles prepared using the co-precipitation method*, Ceram. Int.* 39, 5235–5239
48. Hammad, T. M., et al. (2015). surface morphological and optical properties of PVA passivated PbS nanoparticles, *Journal of Luminescence,* 157, 88–92
49. Vijaya, J. Judith, Sekaran, G. & Bououdina, M. (2014).*Ceram. Int.* 41, 15
50. Gayathri Manju. B. & Rajh, P. "Green Synthesis of Nickel–Copper Mixed Ferrite Nanoparticles: Structural, Optical, Magnetic, Electrochemical and Antibacterial Studies," *Journal of ELECTRONIC MATERIALS.* https://doi.org/10.1007/s11664-019-07603-x.
51. Wang, Y.S., Thomas, P.J. & Brien, P. (2006). Optical properties of ZnO nanocrystals doped with Cd, Mg, Mn, and Fe ions, *J. Phys. Chem.* B 110, 21412https://doi.org/10.1021/jp0654415.
52. Chen, Z.C. et al. (2007). Initial study on the structure and optical properties of Zn1−xFexO films, Thin Solid Films. 515, 5462-5465
53. Ahmed, A.S. et al. (2011). Band gap narrowing and fluorescent properties of nickel doped SnO2 nanoparticles*, J. Lumin.* 131, 1-6
54. Hossain, Mohammad S., et al. (2019) Influence of Ni substitution on structural, morphological, dielectric, magnetic and optical properties of Cu–Zn ferrite by double sintering sol–gel technique, *JOURNAL OF ADVANCED DIELECTRICS,* 9, 1950020.
55. Manikandan, A., Durka, M. & Antony, S.A. (2015). one-pot flash combustion synthesis, structural morphological and opto-magnetic properties of spinel MnxCo1−xAl2O4(x =0,0.3 and 0.5) nanocatalysts*, J. Supercond. Nov. Magn.* 28, 209-218
56. Manikandan, A., Durka, M. & Antony, S.A. (2015). Role of Mn2+ doping on structural, morphological, and opto-magnetic properties of spinel MnxCo1−x Fe2O4(x = 0.0, 0.1, 0.2, 0.3, 0.4, and 0.5) nanocatalysts, *J. Supercond. Nov. Magn*. 28, 2047-2058
57. Godlyn, A.A. et al. (2017). Enhanced opto-magneto properties of NixMg1–x Fe2O4 (0.0 ≤x ≤ 1.0) ferrites nano-catalysts, *J. Nanoelectron. Optoelectron.* 12, 1326-1333
58. Manikandan, A. et al. (2015). A simple combustion synthesis and optical studies of magnetic Zn1–xNixFe2O4 nanostructures for photoelectrochemical applications*, J. Nanosci. Nanotechnol.* 15, 4948-4960
59. Pan, W. et al. (2012). Effect of Zn substitution on morphology and magnetic properties of CuFe2O4 nanofibers, *J. Mater. Chem. Phys.* 134, 1097
60. Chinnasamy, C. N. et al. (2001). *Phys. Rev.* B 63, 184108
61. Zaki, H. M. (2012). *Physica B* 407, 2025
62. Hoque, S. M., Choudhury, A. & Islam, F. (2002). *J. Magn. Magn. Mater.* 251, 292.
63. Anh, L. N. et al. (2015). *J. Alloys Compd.* 647, 419
64. Rais, A., et al. (2014). *Ceramics International* 40, 14413-14419
65. Moradmard, H. Et al. (2015). "Structural, magnetic and dielectric properties of magnesium doped nickel ferrite nanoparticles" *J. Alloys Compd.* 650, 116–22
66. Gabal, M.A., Al Angari, Y.M. & Kadi, M.W. *Polyhedron*(2011). 30, 1185-1190
67. Lenin, N. et al. (2018). *Ceram. Int.* 44, 21866
68. Baldi, G. et al. (2007). Cobalt ferrite nanoparticles: The control of the particle size and surface state and their effects on magnetic properties, *J. Magn. Magn. Mater.,* 311, 10–16
69. Balavijayalakshmi, J., Suriyanarayanan, N. & Jayaprakash, R. (2015). Role of copper on structural, magnetic and dielectric properties of nickel ferrite nano particles. *J. Magn. Magn. Mater.* 385, 302–7